White Rose Research Online

eprints@whiterose.ac.uk
https://eprints.whiterose.ac.uk
Universities of Leeds, Sheffield and York

Deposited via The University of Leeds.

White Rose Research Online URL for this paper:
https://eprints.whiterose.ac.uk/id/eprint/117740/

Version: Accepted Version

Article:
Ebrahim, M, Ortega, A, Delbosc, N et al. (2017) Simulation of the spreading of a gas-propelled micro-droplet upon impact on a dry surface using a lattice-Boltzmann approach. Physics of Fluids, 29 (7). 072104. ISSN: 1070-6631

https://doi.org/10.1063/1.4989546

© 2017, the Author(s). Published by AIP Publishing. This is an author produced version of a paper accepted for publication in Physics of Fluids. Uploaded in accordance with the publisher's self-archiving policy.

Reuse
Items deposited in White Rose Research Online are protected by copyright, with all rights reserved unless indicated otherwise. They may be downloaded and/or printed for private study, or other acts as permitted by national copyright laws. The publisher or other rights holders may allow further reproduction and re-use of the full text version. This is indicated by the licence information on the White Rose Research Online record for the item.

Takedown
If you consider content in White Rose Research Online to be in breach of UK law, please notify us by emailing eprints@whiterose.ac.uk including the URL of the record and the reason for the withdrawal request.

Simulation of the spreading of a gas-propelled micro-droplet upon impact on a dry surface using a lattice-Boltzmann approach

Mahsa Ebrahim*, Alfonso Ortega*, Nicolas Delbosc†,
Mark C.T. Wilson† and Jonathan L. Summers†
* *Laboratory for Advanced Thermal and Fluid Systems,*
Villanova University, Villanova, PA, USA, 19085
† *Institute of Themofluids, School of Mechanical Engineering,*
University of Leeds, Leeds, LS2 9JT, UK

(Dated: June 5, 2017)

Abstract

Spray cooling is one of the most promising methods of cooling high heat flux electronics. Depending on the type of the nozzle, spray cooling can be categorized as single phase or two phase. In the latter, which is known to be more effective, a secondary gas is used to further pressurize the liquid and form smaller droplets at higher velocities. The gas is also assumed to assist the spreading phase by imposing normal and tangential forces on the droplet free surface which adds to the complicated hydrodynamics of the droplet impact. Moreover, the order of magnitude of droplet size in spray cooling is $10^{-6}m$ thereby introducing a low Weber and Reynolds numbers impact regime which heretofore has not been well understood. A 3D lattice Boltzmann method was implemented to simulate the impact of a single micro-droplet on a dry surface in both ambient air and under a stagnation gas flow. Two cases were closely compared and correlations were proposed for the instantaneous spreading diameter. Contrary to recent findings at higher impact We and Re, it was found that stagnation flow only significantly affects the spreading phase for $Ca^* \geq 0.35$ but has little influence on the receding physics.

INTRODUCTION

Droplet impingement on solid and liquid surfaces have been extensively investigated due to the numerous applications in ink-jet printing, paint coating, plasma spraying, metal forming, internal combustion engines, microfabrication and spray cooling of high heat flux surfaces. In the latter application, understanding the fundamental hydrodynamics is of utmost importance in order to avoid dry out or excessive liquid accumulation. Vapor-assisted spray cooling in which liquid droplets are atomized with a secondary pressurized gas phase has more complicated physics and has not yet been fully investigated and understood. This technique is known to have a higher heat transfer coefficient [1, 2] since smaller droplets at higher velocities are formed and impact the surface under a stagnation jet flow. The gas jet flow is also assumed to thin the liquid film by imposing shear stress forces. The current investigation of which this work is a part is designed to experimentally and computationally investigate the basic physics of droplet impingement under the influence of a propellant gas. This paper presents the results of a lattice-Boltzmann numerical study that has allowed the exploration of physics at micro-scale droplet diameters that are common in industrial spray systems. Extension of the regime of investigation to micro scaled droplets augments the previous investigations by the author's team [3, 4] for meso-scale droplets.

Considerable experimental work has been carried out to investigate the hydrodynamics of the impact of a liquid millimeter size droplet on a dry solid surface. [5–11]. Many parameters were found to affect the dynamics of the impact, including: impact velocity, liquid properties (density, viscosity, surface tension, and Newtonian or non-Newtonian rheology), surface roughness and wettability, droplet size, angle of the impact, surrounding pressure, and surface temperature. Depending on the impact condition, different outcomes can result such as fine deposition, spreading splash, receding break up or bounce back [12]. It has been observed that maximum spreading is augmented as impact velocity increases [7–9]. Viscous droplets are found to spread less, and a noticeably slower receding phase was detected for non-Newtonian droplets [8, 9, 11]. It is known that larger droplets and high surface roughness increase the possibility of splashing [5, 6] while lower surrounding pressure suppresses the droplet disintegration for the same impact conditions [10]. A review of the rich literature of droplet impact on a dry solid surface can be found in [13].

For practical reasons, most of the investigations in the literature are performed on mil-

limeter size droplets, whereas in spray cooling droplet sizes are three orders of magnitude smaller [14, 15]. These micrometer size droplets result in an impact regime of low Weber (We) number and low Reynolds (Re) number regardless of the magnitude of the impact velocity. Son et al. [16] experimentally studied the impact of inkjet droplets at low We and Re numbers. They found that the impact dynamics for low We numbers were different from the moderate to high We numbers. Droplet impingement under a stagnation jet flow, as occurs in the gas assisted spray cooling technique, has undergone little investigation and is not fully understood. The interaction between the stagnation jet and droplet surface and including especially the influence of the jet normal and shear forces on the hydrodynamics of the impact add to the complexity of the problem. An experimental and numerical investigation on the impact of a gas propelled millimeter size water droplet on a heated surface was performed by Diaz and Ortega [4, 17]. Enhancement was observed in the maximum spreading factor of sub-millimeter droplets due to the stagnation pressure on the droplet surface for $\mathrm{We}_{gas}/\mathrm{We}_{drop} > 0.1$. Ebrahim and Ortega [3] investigated gas propelled droplet impact at considerably higher We numbers ($300 \geq \mathrm{We}_{drop} \geq 6000$) and found that while the propellant gas does not enhance spreading, it does retard both receding and the onset of splash.

In the present work, a 3D lattice Boltzmann simulation is developed to study the impact of a micro-sized droplet in the low We and Re numbers impact regime ($\mathrm{We} < 45$, $\mathrm{Re} < 450$). The simulation is validated with the experimental data of Briones et al. [18]. The impact of micro-sized droplets in free-fall in ambient air and under a stagnation air flow are modeled in order to study the hydrodynamics of unassisted and gas assisted droplet impact, respectively, at these very low droplet diameters.

LATTICE BOLTZMANN METHOD

Recently, the latice Boltzman method (LBM) has shown to be a powerful method for the numerical simulation of complex flows such as porous media flows and multiphase flows. The LBM is a mesoscopic method that covers the gap between the microscopic molecular dynamics and the macroscopic fluid mechanics. The mesoscopic nature of LBM yields a practical way of implementing microscopic dynamics between fluid-fluid and fluid-solid interactions as it solves the discrete form of the Boltzmann equation in the bulk flow [19].

In the LBM, the fluid field consists of similar particles that are allowed to move in specific directions and the flow motion is captured by a set of distribution functions. The studies of LBM are numerous and therefore here we only review and discuss the Multiphase LBM suitable for current investigations.

Different methods for multiphase LBM simulations have been developed and can be categorized as chromodynamic (Gunstensen et al. [20]), free energy (Swift et al. [21]), pseudo-potential (Shan and Chen [22]) and finite density (He et al. [23]). The Shan and Chen model is the most popular multiphase LB model because of its simplicity and computational efficiency. A complete review of the pseudo-potential models can be found in Chen et al. [24]. The advantages of the He et al. model are its thermodynamic consistency and the ability to vary densities and viscosities independently. Its use is restricted to nearly incompressible single-component flows with two phases.

In the present work, the method of He et al. [23] is implemented to simulate the impact of a free-falling droplet in ambient air and the impact of a droplet under a stagnation air jet flow. This method is briefly explained in the following section. Further details of this method can be found in [23].

Method of He et al.

Using the Bhatnagar-Gross-Krook single relaxation time approximation, the general Boltzmann equation for non-ideal fluids can be written as [25]

$$\frac{\partial f}{\partial t} + \mathbf{e}.\nabla f = -\frac{f - f^{eq}}{\tau} + \frac{(\mathbf{e} - \mathbf{v}).(\mathbf{F} + \mathbf{G})}{\rho RT} f^{eq} \tag{1}$$

where $\mathbf{F}$ is the effective molecular interaction, $\mathbf{G}$ is the gravity force, R is the gas constant, T is the temperature, $\mathbf{e}$ and $\mathbf{v}$ are the microscopic (i.e. molecular) and macroscopic velocities, respectively, ρ is the macroscopic fluid density, and $f(\mathbf{x}, \mathbf{e}, t)$ is the single-particle probability distribution function, with local equilibrium value given by

$$f^{eq}(\mathbf{v}) = \frac{\rho}{(2\pi RT)^{\frac{3}{2}}} \exp\left(\frac{-(\mathbf{e} - \mathbf{v})^2}{2RT}\right) \tag{2}$$

The effective molecular interaction force can be defined based on the mean-field approximation [23], as follows

$$\mathbf{F} = -\nabla\psi + \mathbf{F}_s \tag{3}$$

where the first term on the right hand side of Eq. 3 represents the interaction due to the non-ideal part of the equation of state (EOS) and the second term associated with the surface tension force, as follows

$$\psi(\rho) = P - \rho RT, \qquad \mathbf{F}_s = \kappa\rho\nabla\nabla^2\rho \tag{4}$$

where κ determines the strength of surface tension force and in this work pressure, P, is obtained from the Carnahan and Starling EOS [26]. Since the evolution of $\nabla\psi$ across the interface is large, and hence evaluation of the inter molecular force can lead to instability, He et al. [23] introduced an auxiliary pressure distribution function given by

$$g = fRT + \psi(\rho)\Gamma(0) \tag{5}$$

where

$$\Gamma(\mathbf{v}) = \frac{f^{eq}(\mathbf{v})}{\rho} \tag{6}$$

The macroscopic pressure and velocity can then be obtained by integrating the g distribution function as follows

$$P = \int g d\mathbf{e}, \qquad \rho RT\mathbf{u} = \int \mathbf{e} g d\mathbf{e} \tag{7}$$

He et al. [23] proposed a mass index function of $\phi = \int f d\mathbf{e}$, where f is obtained from Eq. 1. The role of the ϕ is to keep track of the two separate phases, and hence the shape and position of the interface between them. The densities and viscosities of the phases of interest are mapped onto ϕ and are determined by a simple interpolation of the index function, given by

$$\rho = \rho_g + \frac{\phi - \phi_g}{\phi_l - \phi_g}(\rho_l - \rho_g), \qquad \nu = \nu_g + \frac{\phi - \phi_g}{\phi_l - \phi_g}(\nu_l - \nu_g) \tag{8}$$

where ρ_l and ρ_g are liquid and vapor densities, respectively. Similarly, ν_l and ν_g stand for the liquid and vapor viscosities, and ϕ_l and ϕ_g are the minimum and maximum values of

the index function [23].

To proceed with a numerical scheme, the above equations must be discretized to produce the corresponding lattice Boltzmann equations. This involves discretizing the microscopic velocity space into a set of discrete velocities, $\mathbf{e}_i$, and evaluating the moment integrals, Eq. 7, by quadrature [19, 23]. This discretization of velocity is linked to the discretization of space by defining a lattice where the spacing between neighboring nodes is given by $\mathbf{e}_i\delta t$, where δt is the time step. In this study, the standard D3Q19 lattice is used, in which each node has links to its 18 nearest neighbors

Following the analysis of He et al [23], final discrete forms of the evolution equations with the change of variables of $\bar{f}_i = f_i + \tilde{\mathbf{F}}_i$ and $\bar{g}_i = g_i + \tilde{\mathbf{G}}_i$ (to create an explicit scheme), are given as

$$\bar{f}_i(\mathbf{x} + \mathbf{e}_i\delta t, \mathbf{e}_i\delta t) - \bar{f}_i(\mathbf{x}, \delta t) = -\frac{1}{\tau}(\bar{f}_i(\mathbf{x}, \delta t) - f_i^{eq}(\mathbf{x}, \delta t)) - \frac{2\tau - 1}{\tau}\tilde{\mathbf{F}}_i \tag{9}$$

$$\bar{g}_i(\mathbf{x} + \mathbf{e}_i\delta t, \mathbf{e}_i\delta t) - \bar{g}_i(\mathbf{x}, \delta t) = -\frac{1}{\tau}(\bar{g}_i(\mathbf{x}, \delta t) - g_i^{eq}(\mathbf{x}, \delta t)) - \frac{2\tau - 1}{\tau}\tilde{\mathbf{G}}_i \tag{10}$$

where

$$\tilde{\mathbf{F}}_i = \frac{\delta t}{2RT}(\mathbf{e}_i - \mathbf{v})\nabla\psi(\phi)\Gamma_i(\mathbf{v}) \tag{11}$$

$$\tilde{\mathbf{G}}_i = -\frac{\delta t}{2}(\mathbf{e}_i - \mathbf{v})[\Gamma_i(\mathbf{v})(\mathbf{F}_s + \mathbf{G}) - (\Gamma_i(\mathbf{v}) - \Gamma_i(0)).\nabla\psi(\rho)] \tag{12}$$

and

$$\Gamma_i(\mathbf{v}) = \omega_i\left(1 + \frac{3}{c^2}(\mathbf{e}_i.\mathbf{v}) + \frac{9}{2c^4}(\mathbf{e}_i.\mathbf{v})^2 - \frac{3}{2c^2}\mathbf{v}^2\right) \tag{13}$$

where $c = \sqrt{3RT}$ and ω_i are weights arising from the quadrature. The corresponding discrete equilibrium distribution functions are given by $f_i^{eq}(\mathbf{v}) = \rho\Gamma_i(\mathbf{v})$ and $g_i^{eq}(\mathbf{v}) = \rho RT\Gamma_i(\mathbf{v}) + \psi(\rho)\Gamma_i(0)$.

The macroscopic variables can be computed from

$$\phi = \sum_i \bar{f}_i \tag{14}$$

$$P = \sum_i \bar{g}_i - \frac{1}{2}\mathbf{v}.\nabla\psi(\rho)\delta t \tag{15}$$

$$\rho RT\mathbf{u} = \sum_i \mathbf{e}_i\bar{g}_i + \frac{RT}{2}(\mathbf{F}_s + \mathbf{G})\delta t \tag{16}$$

where ρ is obtained by interpolating the index function through Eq. 8 and $\psi(\phi)$ is computed from Eq. 4 using the Carnahan and Starling EOS, where $b = 4$:

$$\psi(\phi) = P - \frac{\phi}{3} = \phi^2\left(\frac{2RT(2-\phi)}{(1-\phi)^3} - 4\right) \tag{17}$$

It should be noted that the choice of a in the EOS affects the ϕ_l and ϕ_g through the coexistence curve and Maxwell's equal area rule. $\psi(\rho)$ is calculated using the numerically obtained P from the simulation. Since fluid kinetic viscosity is coupled with the relaxation time ($\nu = c_s^2\delta t(\tau - \frac{1}{2})$) and the index function (Eq. 8), the relaxation time varies across the interface. Moreover, a six point stencil finite difference approach with a second order accuracy is used to calculate the gradient of $\psi(\rho)$.

The Wettability of Wall

To model the fluid-solid interaction (wall wettability) in the He et al. [23], Davies et al. [27] proposed a wetting boundary condition by applying the surface affinity concept [28] to the index function. The surface affinity, χ is defined as

$$\chi = \frac{\phi - \frac{1}{2}(\phi_l + \phi_g)}{\phi_l - \phi_g} \tag{18}$$

such that $\chi = -1$ and $\chi = +1$ represent hydrophobic and hydrophilic surfaces, respectively. Iwahara et al. [28] related the equilibrium contact angle to the surface affinity through the Young's equation, as follows

$$\cos(\theta_{eq}) = \frac{\chi}{2}(3 - \chi^2) \tag{19}$$

Therefore, the equilibrium contact angle, which is related to the wettability of the solid surface, specifies the wall surface affinity. Then, this value of surface affinity prescribes the index function of the wall (ϕ_s) that affects the $\psi(\phi)$ via Eq. 17. The gradient of $\psi(\phi)$ at the solid wall can be numerically calculated using a non-equilibrium bounce back boundary condition at the wall. This gradient is finally used in the force terms (Eq. 11 and 12) of the lattice Boltzmann equations. Further details of the wetting boundary condition can be found in [27].

RESULTS AND DISCUSSION

Three-dimensional micro-meter size water droplets were simulated for a density ratio of $\rho_l/\rho_g = 10$ and interface thickness of 1.5. Note that this density ratio is substantially lower than the water/air ratio of the experiments used for validation. As with many diffuse interface/LB models, setting the density ratio too high leads to numerical instability and simulation failure. Here, a value is chosen at the upper end of the stable range for this model, where predictions are found to become insensitive to the specific value of the density ratio. In the first set of results, the droplet impingement in free-fall in ambient air was investigated for different impact conditions. In the second set, the impingement under a stagnation air flow was modeled and the two cases were compared.

Droplet impact in free-fall in ambient air

The simulations were initialized with a droplet positioned in the center of the domain with a downward velocity of V_0. Periodic boundary conditions were set for the side boundaries, and the top and bottom were set to wetting wall boundary condition. The schematic of the problem domain and boundary conditions are shown in Fig. 1.

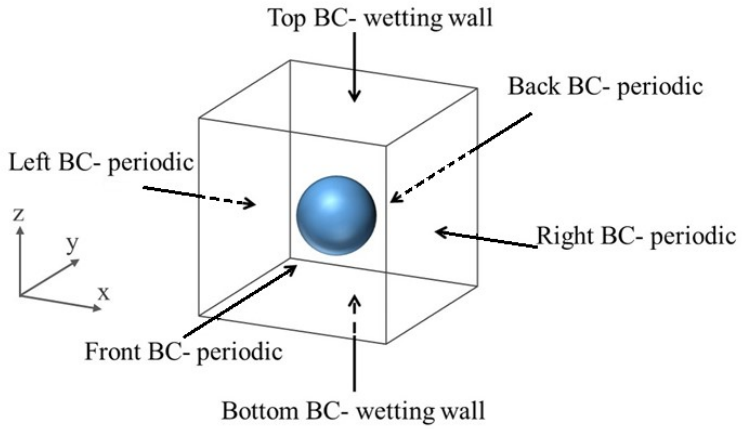

FIG. 1: Schematic of the problem domain and boundary conditions

The range of the parameters varied in the simulations are listed in Table I, including the Weber number (We), Reynolds number (Re), Ohnesorge number (Oh), Capillary number (Ca), droplet initial diameter (D_0), droplet impact velocity (V_0), and the equilibrium contact angle (θ_{eq}). The We, Re, Oh and Ca numbers are defined as

$$\mathrm{Re} = \frac{\rho V_0 D_0}{\mu}, \qquad \mathrm{We} = \frac{\rho V_0^2 D_0}{\sigma} \tag{20}$$

$$\mathrm{Oh} = \frac{\sqrt{\mathrm{We}}}{\mathrm{Re}} = \frac{\mu}{\sqrt{\rho \sigma D_0}}, \qquad \mathrm{Ca} = \frac{\mathrm{We}}{\mathrm{Re}} = \frac{\mu V_0}{\sigma} \tag{21}$$

TABLE I: Variation of different parameters in the simulations

	We	Re	Oh $\times 10^3$	Ca	$D_0[\mu m]$	$V_0[m/s]$	$\theta_{eq}[^\circ]$
min	1.4	40	8.3	0.035	2.7	1.2	30
max	42	410	70.7	0.102	200	11	98

Validation

The experimental data of Briones et al. [18] was used to validate the three-dimensional LBM simulation of this study. Operating conditions for each impact case are listed in Table II and were exactly matched in each simulation. The maximum spreading factor, $\xi_{max} = D_{max}/D_0$, of the LBM simulation is compared to the experimental data in Fig. 2 with respect to the dimensionless time $\tau = tV_0/D_0$. It can be seen that the simulation results agree well with the experiments to within $\pm 5.5\%$ error. The instantaneous dimensionless droplet diameter during the spreading phase, $\xi = D/D_0$, for the two impact cases B and D, is illustrated in Fig. 3. Good agreement is observed for $\tau > 0.4$. For very early times, $\tau < 0.2$, the LBM simulations strongly under-predict the data. The good agreement at later times, and the ability to predict the maximum spreading diameter indicate that the LBM approach can reveal droplet impact physics with a good degree of confidence during the majority of the spreading regime.

Spreading Regime in Free Fall

As pointed out by Ebrahim and Ortega [3], immediately after impact, the droplet experiences a collapsing regime, in which a spherical droplet begins to deform to a lamella

TABLE II: Operating conditions of the experimental data [18]

droplet	$D_0[\mu m]$	$V_0[m/s]$	We	Re	Oh $\times 10^3$	$\theta_{eq}[^\circ]$
A	40.7	1.56	1.4	63.4	26	87.09
B	35.6	3.02	4.5	107.3	28	79.04
C	55.4	2.45	4.6	135.5	22	50.32
D	36.6	4.02	8.2	146.8	28	65.66
E	32.2	5.14	11.8	165.2	29	64.45
F	33.4	4.97	11.4	165.7	29	66.69

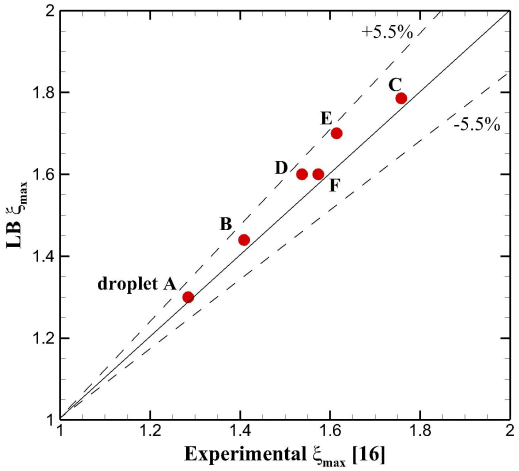

FIG. 2: Maximum spreading factor of LBM simulation vs. experimental data [18]

with a defined contact line. For moderate to high impact conditions, this regime has very short duration and therefore is usually neglected. After the formation of the lamella, the spreading phase continues until the droplet initial kinetic energy is completely converted to surface tension energy of the stretched lamella and dissipated by the wall shear stress. After the droplet reaches its maximum spreading diameter, the receding phase is initiated by the surface tension force that induces the retraction of the initially stretched droplet until it achieves a new static equilibrium state. Depending on the surface wettability and temperature, the droplet may continue to recede until it rebounds completely or partially from the surface. The equilibrium state is eventually achieved after experiencing a number of oscillations between the spreading and receding phase. This paper focuses only on the spreading phase. The continuing study is focusing on the receding phase. Figure 4 illustrates the time elapsed images of the simulations during the spreading phase for two impact conditions.

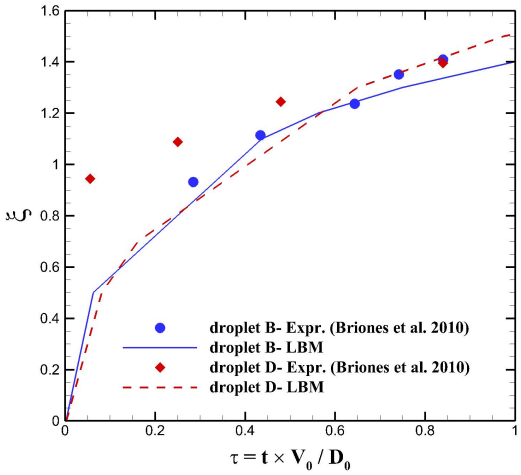

FIG. 3: Instantaneous spreading factor

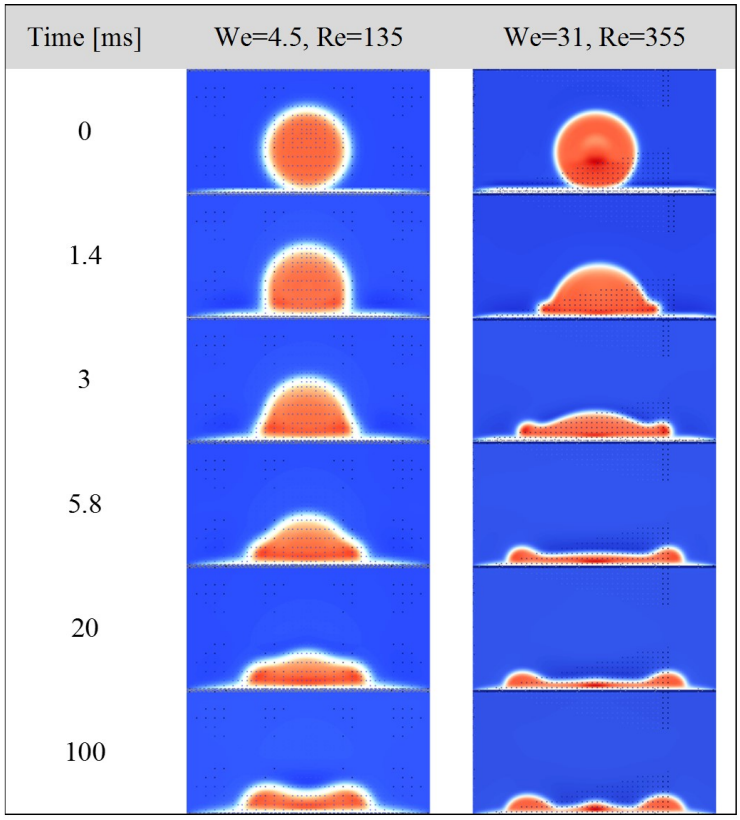

FIG. 4: Time elapsed images of the LBM simulations

Numerous analytic models have been proposed to determine the maximum spreading diameter for the moderate to high impact We and Re numbers [29–33]. There are however few dynamic models to compute the instantaneous droplet diameter [34–36]. Several of these models are presented in Table III and are compared against the experimental data

of Briones et al. [18], Figure 5 presents the error in predicting the maximum spreading diameter, ξ_{max}, using these models. The correlation of Scheller and Bousfield [37] and the model of Son et al. [16] are accurate for all case studies ($1 < \mathrm{We} < 12$) to within $\pm 25\%$. The models of Attane et al. [34] and Pasandideh-Fard et al. [30] are reasonable for $8 < \mathrm{We}$. The remaining models fail to adequately predict the behavior of these micro-droplets. One possible reason for the failure of these models is that they are based on the energy balance approach, in which a cylindrical shape droplet is assumed immediately after impact. Son et al. [16] speculated that this assumption is not valid for micrometer size droplet impact, because no lamella formation was observed in their experiments performed in the low We and Re number impact regime. Those observations are confirmed in Fig. 4, where low and high impact conditions are compared. Therefore a simple model or correlation to predict the dynamic spreading diameter within the low We and Re numbers impact regimes must acknowledge these physics and remains undeveloped to now.

TABLE III: Analytic models to predict maximum spreading diameter

Model	Equation
Chandra and Avedisian [29]	$\frac{3}{2}\frac{\mathrm{We}}{\mathrm{Re}}\xi_{max}^4 + (1-cos\theta)\xi_{max}^2 - \left(\frac{\mathrm{We}}{3}+4\right) = 0$
Yang [31]	$\frac{\mathrm{We}}{2} = \frac{3}{2}\xi_{max}^2\left(1+\frac{3\mathrm{We}}{\mathrm{Re}}\left(\xi_{max}^2 ln\xi_{max} - \frac{\xi_{max}^2-1}{2}\right)\left(\frac{\mu_{drop}}{\mu_{wall}}\right)^{0.14}\right) - 6$
Jones [32]	$\xi_{max} = \left(\frac{\mathrm{We}}{6}\right)^{0.5}$
Madejski [33]	$\frac{3\xi_{max}^2}{\mathrm{We}} + \frac{1}{\mathrm{Re}}\left(\frac{\xi_{max}}{1.2941}\right)^5 = 1$
Pasandideh-Fard et al. [30]	$\xi_{max} = \sqrt{\frac{\mathrm{We}+12}{3(1-cos\theta)+4\left(\frac{\mathrm{We}}{\sqrt{\mathrm{Re}}}\right)}}$
Attane et al. [34]	$\frac{1}{2}\frac{d}{dt}(\left(\left[\frac{1}{2}+\frac{1}{27}\frac{1}{r^6}\right]\left(\frac{dr}{dt}\right)^2\right) + \frac{1}{dt}[r^2(1-cos\theta_{eq})+\frac{1}{3r}] + \frac{\Lambda}{2}\mathrm{Oh}r^2\left(\frac{dr}{dt}\right)^2$
Son et al. [16]	$\xi_{max} = \sqrt{\frac{\mathrm{We}+12}{3(f_s-cos\theta)+4\left(\frac{\mathrm{We}}{\sqrt{\mathrm{Re}}}\right)}}$, $f_s = 1+[1-\frac{cos\theta}{cos(90-\theta)}]^2$
Scheller and Bousfield [37]	$\xi_{max} = 0.61(\mathrm{Re}^2\mathrm{Oh})^{0.133}$

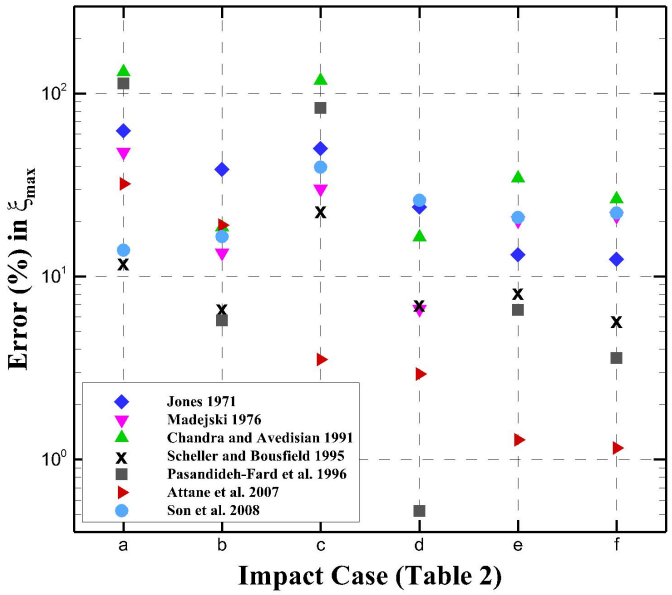

FIG. 5: Comparison of analytical models in Table III with the experimental data of Briones et al. [18], model of Yang [31] does not have real roots for these case studies

Correlation for spreading phase

In order to propose a correlation for the spreading phase it is essential to distinguish the correct time and length scales to properly collapse and normalize data. Therefore, the first step is to find and study the major dimensionless groups and parameters that individually affect the spreading dynamics. As mention previously, the main dimensionless groups describing the hydrodynamics of the droplet impact are Re, We, Oh and Ca numbers. Note that Oh and Ca are not independent; the key dimensionless numbers are clearly We and Re. In comparing micro (micrometer size) and macro (millimeter size) droplet impingement it is necessary to match any two of these dimensionless groups. It is possible to match impact We number of micro and macro size droplets by varying the impact velocity, but the Re number of a micro droplet will be at least one order of magnitude smaller than that of the macro droplet, regardless of the impact velocity. The flow therefore will be dominated by low Re number physics which would tend towards creeping flow rather than collapsing and flattening to a lamella. This is substantiated in the experiments of Son et al. [16] and likely contributes to the failure of most of the analytic models.

Surface wettability, which is commonly defined in terms of equilibrium contact angle, can also independently affect impact dynamics. This phenomenon depends on the chemical

properties of the surface and the liquid [38, 39] and therefore the wettability of a pure liquid varies on different surfaces. It should be noted that, surface wettability is often confused with surface tension modification. The effect of surface tension modification is captured in We number.

The individual effects of We and Re numbers obtained from lattice Boltzmann simulations are shown in Figs. 6a and 6b . Droplet diameter and impact velocity are adjusted such as to maintain one dimensionless number constant while varying the other. The separate influences of We and Re numbers illustrate the distinct effects of droplet surface tension and viscosity on the spreading phase. The effect of We number is illustrated in Fig.6a. When We number is increased, the rate of the spreading phase is not significantly affected because the enhancement in We number is primarily due to the decrease in surface tension. Therefore, for a given kinetic energy and viscous dissipation, a weakened opposing surface tension force will cause the spreading phase to continue longer without significant change in the rate and lead to a larger spreading diameter. Figure 6b demonstrates the significant influence of Re number on the dynamics of the impact due primarily to the influence of the initial droplet kinetic energy. Rioboo et al. [7] made similar observations for the individual effects of We and Re numbers for millimeter-size droplet impact. The influence of surface wettability is illustrated in Fig. 6c. It is clear that as equilibrium contact angle decreases or as the surface becomes more hydrophilic, the rate and the extent of the maximum spreading diameter are enhanced.

Further study of Fig. 6 shows that the dimensionless time, $\tau = t \times \frac{V_0}{D_0}$, fails to normalize the time of the spreading dynamics, except for cases where Re number is varied. Therefore, a more appropriate time scale to normalize the dynamic time must depend on We number and surface wettability, which are both incorporated in the surface tension force. Using the surface tension force and the acceleration it causes during the spreading phase, the spreading time scale, t_s, can be approximated as follows:

$$F_{surfaceTension} \propto M_d \left(\frac{V_0}{t_s} \right) \tag{22}$$

$$\sigma D_0 (1 - \cos\theta) \propto \rho D_0^3 \frac{V_0}{t_s} \longrightarrow t_s \propto \left(\frac{\mathrm{We}}{1 - \cos\theta} \right) \frac{D_0}{V_0} \tag{23}$$

where M_d and V_0 are the mass and initial velocity of the droplet. The time scale, t_s, was

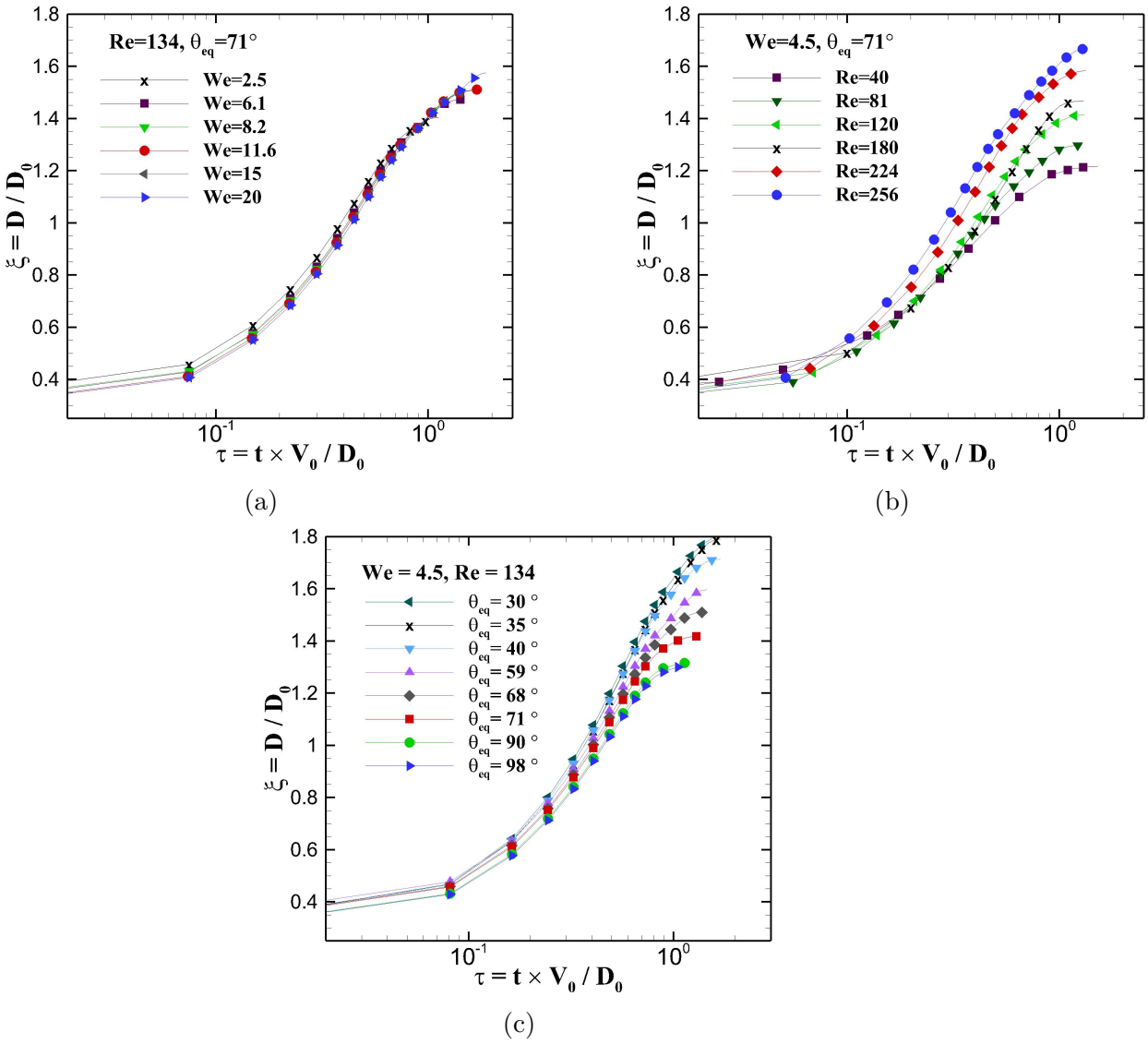

FIG. 6: Instantaneous spreading factor for different impact (a)-We numbers, (b)-Re numbers and (c)- Contact angle

empirically modified based on Eq. 23 to scale the spreading dynamics more accurately as follow

$$t_s = \left(\frac{\mathrm{We}}{1-\cos\theta}\right)^{(\frac{1}{4})} \frac{D_0}{V_0} \tag{24}$$

The new dimensionless time for spreading phase, τ^*, is then defined as

$$\tau^* = \frac{t}{t_s} = \tau \left(\frac{1-\cos\theta}{\mathrm{We}}\right)^{\frac{1}{4}} \tag{25}$$

where $\tau = tV_0/D_0$ is the common dimensionless time previously used in the literature. It

is also clear in Fig. 6 that the non-dimensional length, $\xi = \frac{D}{D_0}$, fails to normalize spreading diameter. Since the dynamic diameter is affected by both the initial droplet size, D_0, and impact velocity, V_0, the maximum spreading diameter, would be a more appropriate length scale because it captures the effects of both initial diameter and velocity. It is also evident from Fig. 6 that the droplet diameter during the spreading phase is more significantly affected by the Re number or viscosity. Hence the dominant terms in approximating the length scale are viscous dissipation and initial kinetic energy. The new length scale, D_s, can be estimated from the time in which all the initial kinetic energy is dissipated and the droplet reaches its maximum spreading diameter, as follows

$$\frac{1}{2} M_d V_0^2 \propto \mu \left(\frac{dv}{dr}\right)^2 D_0^3 t_s \tag{26}$$

$$\rho D_0^3 V_0^2 \propto \mu \left(\frac{D_{max}/t_s}{D_0}\right)^2 t_s D_0^3 \tag{27}$$

Introducing Eq. 24 will lead to

$$D_s \propto D_0 \mathrm{Re}^{\frac{1}{2}} \left(\frac{\mathrm{We}}{1-\cos\theta}\right)^{\frac{1}{8}} \tag{28}$$

It was empirically observed that reducing the power of Re number in Eq. 28 to $\frac{1}{8}$ in order to group the dimensionless numbers together will not significantly affect the normalization results. Therefore, in order to have a neater and simpler curve fit results, Eq. 28 was empirically modified to

$$D_s = D_0 \left(\frac{\mathrm{ReWe}}{1-\cos\theta}\right)^{\frac{1}{8}} \tag{29}$$

The dimensionless length for the spreading phase will thus be

$$\xi^* = \xi \left(\frac{(1-\cos\theta)}{\mathrm{WeRe}}\right)^{\frac{1}{8}} \tag{30}$$

The effectiveness of the introduced dimensionless length, ξ^*, and the dimensionless time, τ^*, is presented in Fig. 7 where the same simulation data of Fig. 6 are normalized using Eqs. 25 and 30. It is clear that the new length and time scale can significantly improve normalizing the impact dynamics. It is also evident that the spreading phase ends at $\tau^*_{max} \approx$

0.79 for all case studies.

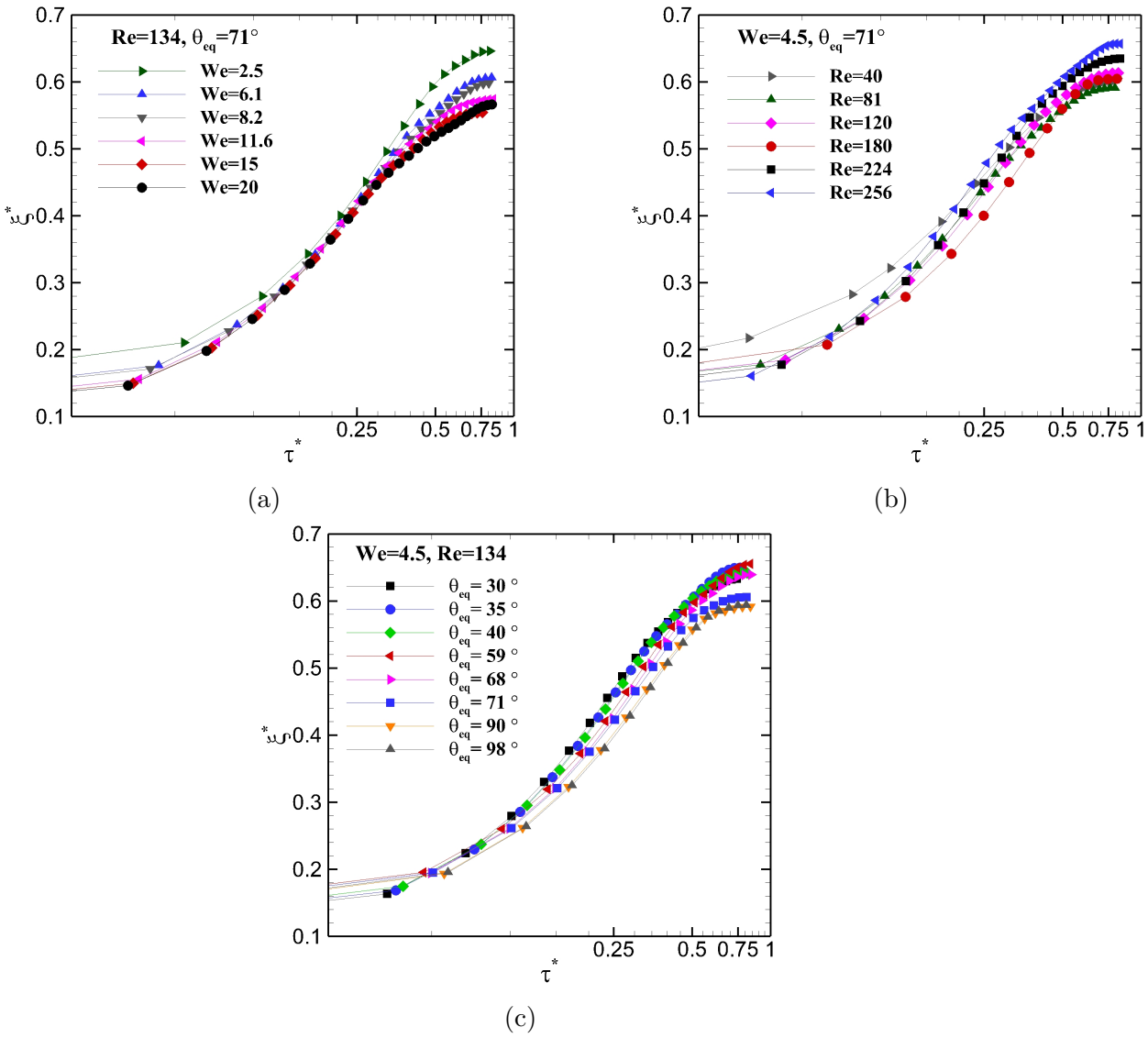

FIG. 7: The effect of new dimensionless length and time in normalizing spreading dynamics for different impact (a)-We numbers, (b)-Re numbers and (c)- Contact angle

The normalized instantaneous spreading phase for numerous impact conditions is illustrated in Fig. 8. A curve fit of the normalized data, given as Eq. 31, is reasonably accurate to predict the instantaneous spreading diameter to within ±16% for low We and Re numbers and for $0.02 \leq \tau^*$. It should be noted that the error is higher for early spreading ($\tau^* \leq 0.02$), because the collapsing process that is usually neglected has different physics and scaling characteristics.

$$\xi^* = (\tau^*)^{\frac{1}{2}}(e^{-0.46\tau^*}) \tag{31}$$

for $2.5 \leq \mathrm{We} \leq 41.8$, $40 \leq \mathrm{Re} \leq 410$, and $0 \leq \tau^* \leq 0.79$. Figure 8 also further confirms that the normalized spreading phase ends at the dimensionless time of $\tau^*_{max} \approx 0.79$ and therefore time to the maximum spreading diameter of any impact condition can be determined as

$$t_{max} = \tau^*_{max} t_s = 0.79 \frac{D_0}{V_0} \left(\frac{\mathrm{We}}{1 - \cos\theta} \right)^{\frac{1}{4}} \tag{32}$$

Since ξ^*_{max} is gained at $\tau^*_{max} = 0.79$, the maximum spreading factor is given as

$$\xi_{max} = 0.6180 \left(\frac{\mathrm{WeRe}}{1 - \cos\theta_{eq}} \right)^{\frac{1}{8}} \tag{33}$$

The instantaneous spreading factor can be calculated by substituting Eq. 30 and Eq. 25 in Eq.31, as follows

$$\xi = \mathrm{Re}^{\frac{1}{8}} \tau^{\frac{1}{2}} \exp\left(-0.46\tau \left(\frac{1 - \cos\theta}{\mathrm{We}} \right)^{\frac{1}{4}} \right) \tag{34}$$

The error in predicting the maximum spreading diameter using Eq. 33 with respect to the experimental data is shown in Fig. 9 and compared against the previous analytical models that were introduced in Table III. Figure 9 further demonstrates the ability of the proposed correlation to reasonably predict the maximum spreading diameter in low impact regimes. The proposed correlations, Eq. 33 and Eq. 34, can be used to reasonably approximate the instantaneous droplet diameter and the maximum spreading diameter, respectively for a droplet impact within the unassisted spray cooling scale, $10 \leq D \leq 100\ \mu m$ and $1 \leq V_0 \leq 25\ m/s$ [14, 15, 40, 41].

Droplet impact under a stagnation air jet

As previously mentioned, vapor assisted spray cooling is known to be more efficient in heat removal than the regular unassisted spray cooling. In this technique, gas-atomizing nozzles with pressurized gas are used to create smaller droplets with higher velocities in a gas stagnation flow field. The gas is hypothesized to thin the liquid film that is formed after the impact of each droplet by imposing shear stress on the droplet surface. Therefore, the heat transfer is speculated to be enhanced due to the formation of a larger contact area and thinner liquid film on the target surface. However, the effect of the gas jet flow on the

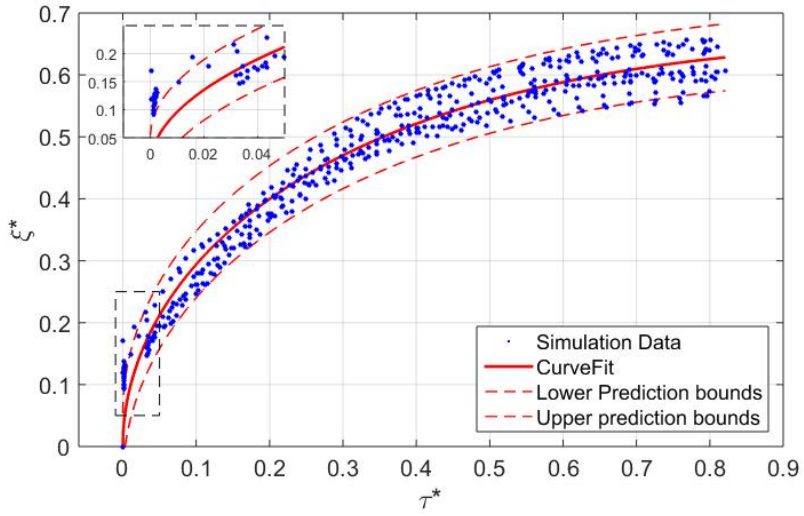

Simulation Data variation:
$2.5 \leq \mathrm{We} \leq 42$
$40 \leq \mathrm{Re} \leq 410$
$30° \leq \theta_{eq} \leq 98°$

FIG. 8: Normalized Instantaneous spreading diameter for free falling droplet in ambient air

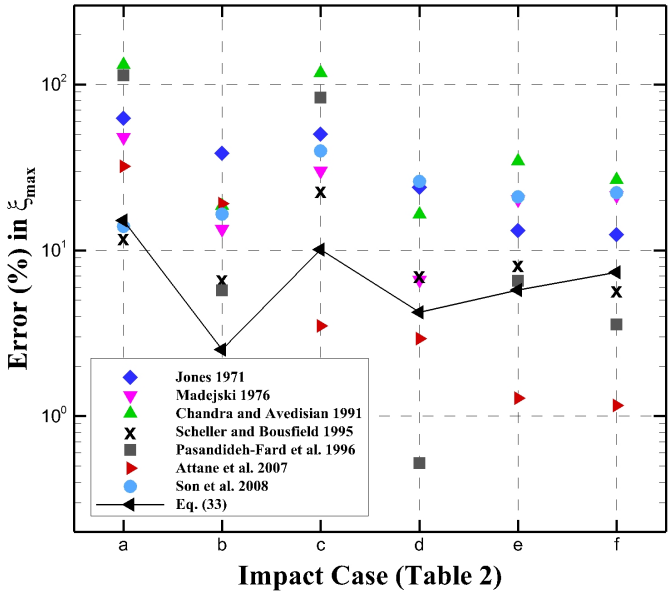

FIG. 9: Comparison of Eq. 33 and analytical models in Table III with the experimental data of Briones et al. [18]

dynamics of the droplet impact is not fully understood.

Effect of the stagnation jet flow

In this section, the impact of a water droplet under an air jet flow is simulated and hence a stagnation jet is added to the spreading phase and boundary conditions are changed

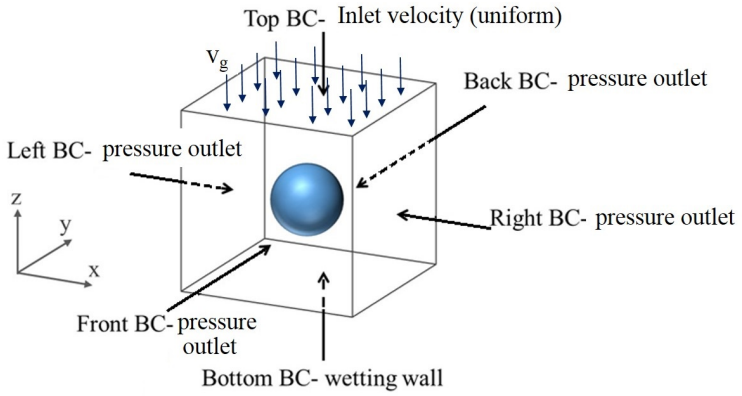

FIG. 10: Schematic of the droplet impact under stagnation jet flow

accordingly. The boundary condition method proposed by Chang et al. [42] and Liu et al. [43] was applied to change the boundaries into inlet-velocity or pressure-outlet boundary conditions. At each boundary, the unknown distribution functions are estimated based on their equilibrium distribution function with an additional correction factor, as follows

$$\bar{f}_i = \bar{f}_i^{eq} + \omega_i Q_f \tag{35}$$

$$\bar{g}_i = \bar{g}_i^{eq} + \omega_i \boldsymbol{e}_i . \boldsymbol{Q}_g \tag{36}$$

where Q_f and $\boldsymbol{Q}_g$ are the correction factors for each boundary and can be determined by satisfying the conservation of mass and momentum, respectively. The top boundary was changed to inlet-velocity, where the density and all the velocity components are known and the pressure is unknown. All the side boundaries were modified to pressure-outlet boundary condition, where the density and pressure are known, velocity components parallel to the boundary are considered zero, and the velocity component perpendicular to the boundary is unknown. Jet-to-surface distance was considered $H/D_0 = 2.5$ and the droplet was initially positioned in the middle of the domain with an initial velocity, V_0. The effect of the jet on the droplet acceleration was neglected due to the fact that the distance travelled by the droplet before the impact is too short. A schematic of the problem domain and boundary conditions is shown in Fig.10.

The effect of jet average velocity is demonstrated in Fig. 11 for the droplet impact condition of Re = 135, $\theta_{eq} = 71.1°$, and We = 4.5 and 14.5, where the gas We number is defined as $\mathrm{We}_g = \rho_g V_g^2 D_0/\sigma$ where V_g is the jet velocity and ρ_g is the gas density. It can be seen in

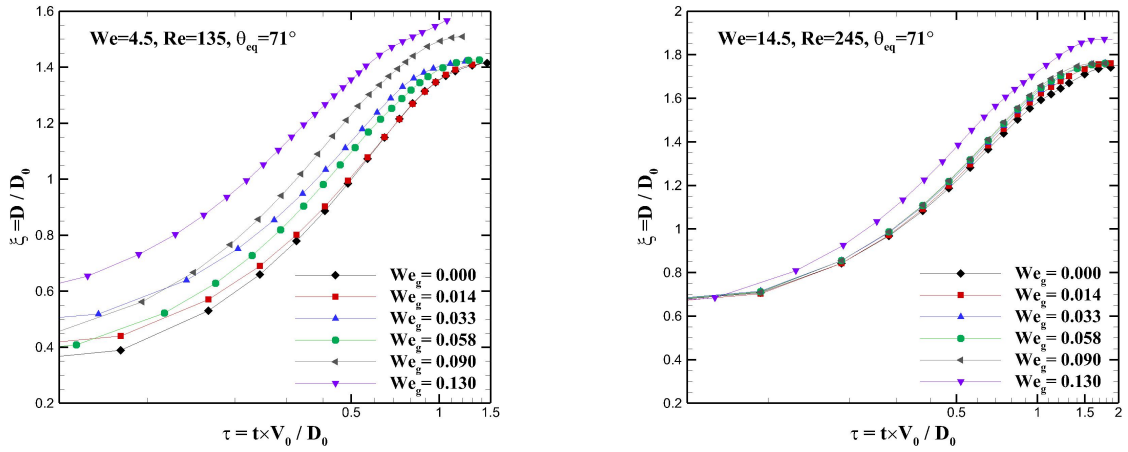

(a) (b)

FIG. 11: Instantaneous spreading factor for different We_g for impact condition of $Re = 245$, and $\theta_{eq} = 71.1°$ (a)- $We = 4.9$ and (b)-$We = 14.9$

Fig. 11a that the stagnation jet does not significantly affect the maximum spreading diameter for $We_g < 0.09$, while considerable enhancement is observed in both the rate and extent of the spreading for $We_g \geq 0.09$. It should be noted that, the gas affects the early spreading phase for $We_g < 0.09$, however, this phase is usually neglected due to its complicated physics and rapid behavior. The same influence can be seen in Fig. 11b, with the exception that the stagnation jet starts to affect the spreading phase for $We_g \geq 0.13$. It is clear that jet shear stress on the droplet surface increases as We_g is augmented. However, jet normal and tangential forces have to be sufficiently strong compared to the droplet spreading kinetic energy in order to affect and assist the maximum spreading diameter.

It is necessary to determine the critical We_g at which the stagnation jet flow starts to influence the spreading phase and further stretches the maximum spreading diameter. Figure 12 represents the normalized results of various impact conditions. It is evident that for $Ca^* \geq 0.35$, a more significant effect is observed in the maximum spreading diameter $\xi_{max-withjet}/\xi_{max} > 1$ and therefore we define Ca^* as the critical effective point given as

$$Ca^* = \frac{We^*}{Re^*} \geq 0.35 \tag{37}$$

where $We^* = \frac{We_g}{We} = \frac{\rho_g V_g^2}{\rho V_0^2}$, $Re^* = \frac{Re_g}{Re} = \frac{\rho_g V_g \mu}{\rho V_0 \mu_g}$, and $Ca^* = \frac{Ca_g}{Ca} = \frac{\mu_g V_g}{\mu V_0}$.

Note that the stagnation jet imposes both normal and tangential forces on the droplet surface during the spreading phase. The normal force is induced by the dynamic pressure

of the jet and the ratio of the dynamic pressure of the jet to the droplet is captured by We^*. The jet viscous force produces the shear or tangential force of the jet and Ca^* shows the ratio of jet viscous force to the droplet. For low impact regime, Ca^* is two order of magnitudes greater than the We^*, indicating that the jet shear force on the droplet surface is stronger and affects the spreading phase more than the jet normal force. Ebrahim and Ortega [3] experimentally observed that the spreading phase was not influenced by the stagnation jet in high to moderate impact regimes, in which both We^* and Ca^* ($Ca^* \leq 0.02$) are negligible. Hence, it could be speculated that for the stagnation jet flow to influence the spreading phase and form a thinner liquid film on the surface, Eq. 37 has to be satisfied.

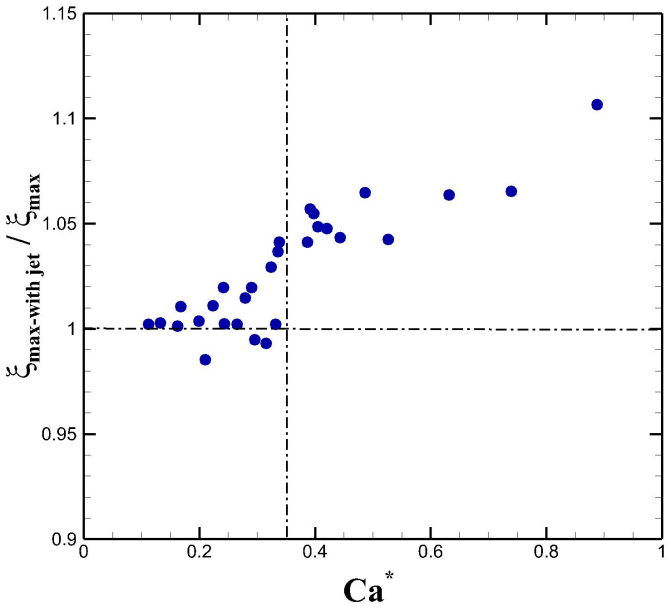

Simulation Data variation:
$2.5 \leq We \leq 42$
$40 \leq Re \leq 410$
$0.014 \leq We_g \leq 0.23$

FIG. 12: Ratio of maximum spreading diameter under the stagnation jet flow to maximum spreading diameter in ambient air

Correlation for spreading phase under stagnation flow

For $Ca^* < 0.35$, where the stagnation jet does not considerably influence the droplet dynamics, Eq. 31 or 34 are still valid. For $Ca^* \geq 0.35$, the main additional physics is the jet viscous force acting on the droplet surface. As discussed previously, Ca^* captures the ratio of jet viscous force to the droplet. Hence, the dimensionless time and length (Eqs. 25 and 30) found for the impact in free-fall were modified to account for the effects of the stagnation jet or Ca^*. The new dimensionless time and length for the impat under the stagnation jet

were found empirically by simply adding the Ca^* to the group of dimensionless numbers in Eqs. 25 and 30:

$$\hat{\tau} = \tau^*(Ca^*)^{\frac{1}{4}} = \tau \left(\frac{(1-\cos\theta)Ca^*}{We} \right)^{\frac{1}{4}} \tag{38}$$

$$\hat{\xi} = \xi^*(Ca^*)^{-\frac{1}{8}} = \xi \left(\frac{1-\cos\theta}{WeReCa^*} \right)^{\frac{1}{8}} \tag{39}$$

Normalized instantaneous droplet diameter under a stagnation jet is shown in Fig. 13 for $Ca^* \geq 0.35$. A curve fit of the data, given as Eq. 40, predicts the instantaneous droplet diameter in the spreading phase accurately up to 15% for $\hat{\tau} \geq 0.15$. This correlation also has higher error for early spreading, because of the collapse process that has different physics and scaling. The error is also more severe for the impact under the stagnation jet, because the jet flow also affects the collapsing process.

$$\hat{\xi} = 0.90\hat{\tau}^{0.33}e^{-0.17\hat{\tau}} \tag{40}$$

for $2.5 \leq We \leq 41.8$, $40 \leq Re \leq 410$, $0.03 \leq We_g \leq 0.2$, and $Ca^* \geq 0.35$.

It is clear in Fig. 13 that the dimensionless time to the maximum spreading diameter under the stagnation jet is $\hat{\tau}_{max} \approx 0.7$. Thus, time to the maximum spreading diameter of a droplet under a stagnation jet can be determined as

$$t_{max} = 0.7\frac{D_0}{V_0}\left(\frac{We}{(1-\cos\theta)Ca^*} \right) \tag{41}$$

Consequently, the maximum spreading factor is determined as

$$\xi_{max} = 0.72\left(\frac{WeReCa^*}{1-\cos\theta} \right)^{\frac{1}{8}} \tag{42}$$

The instantaneous spreading factor for $Ca^* \geq 0.35$ can be computed by substituting Eq. 38 and 39 into Eq. 40, resulting in

$$\xi = 0.90\tau^{0.33}\left(\frac{1-\cos\theta}{We} \right)^{-0.04} Ca^{*0.2}Re^{\frac{1}{8}} \exp\left(-0.17\tau\left(\frac{(1-\cos\theta)Ca^*}{We} \right)^{\frac{1}{4}} \right) \tag{43}$$

The above proposed correlations, Eq.43 and Eq. 42 can be used to approximate the instan-

taneous droplet diameter and the maximum spreading factor in a gas assisted spray cooling regime $10 \leq D \leq 40\ \mu m$ and $10 \leq V_0 \leq 50\ m/s$, respectively [44].

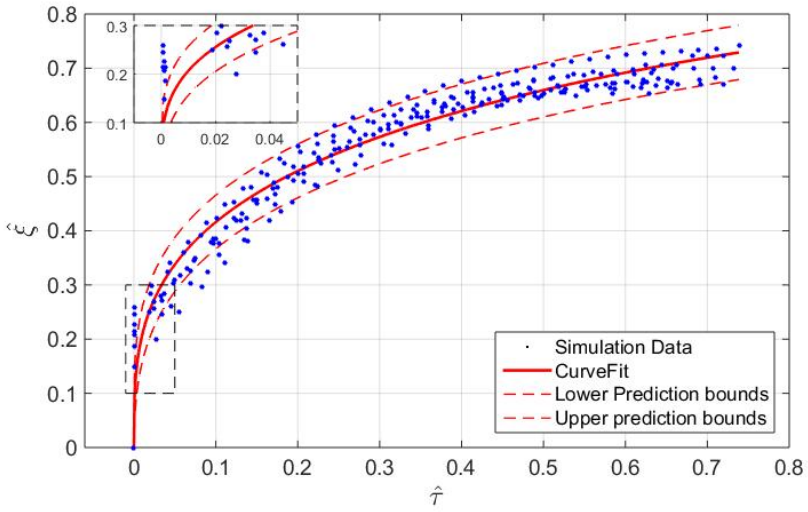

FIG. 13: Normalized Instantaneous spreading diameter for droplet impact under stagnation air jet for $Ca^* \geq 0.35$

TABLE IV: Simulation Data includes:

We	Re	We_g
4.5	135	0.032
4.5	135	0.090
4.5	135	0.130
8.9	190	0.058
8.9	190	0.090
8.9	190	0.130
14.9	245	0.090
14.9	245	0.130
22.3	300	0.130
31.3	355	0.170

CONCLUSIONS

Micrometer droplet impingement was simulated using a 3D lattice Boltzmann method in the low Re and We number regimes. Droplet impact was modeled in the ambient air as well as under a stagnation jet air flow to represent the hydrodynamics of single phase and gas atomized spray cooling, respectively. Numerical data for the impact in the ambient air was verified by the experimental data provided by Briones et al. [18].

The most relevant conclusions can be summarized as follows:

1. We, Re number and surface wettability individually affect the hydrodynamics of the impact and therefore these three parameters must be matched in comparing different situations.

2. Micro-scale droplet impingement which leads to a low impact We and Re regime was found to be distinct from the millimeter-sized or moderate to high impact conditions. Most of the analytic models derived for moderate to high impact regimes fail for the low impact regimes.

3. Simulation data for the impact in ambient air and under a stagnation jet were successfully normalized and correlations for the instantaneous droplet spreading phase of both of the cases were proposed. The correlation for the impact in ambient air can be used to approximate the spreading phase in unassisted spray cooling in which the sprayed liquid droplets impact the surface in the ambient air. However, the spreading phase in gas-assisted spray cooling in which the droplets impact the surface while a stagnation jet flow is imposing normal and tangential forces on them, can be approximated using the correlation for the impact under a stagnation jet.

4. Stagnation jet flow was found to influence the hydrodynamics of the spreading regime when the parameter $\mathrm{Ca}^* = \frac{\mu_g V_g}{\mu V_0} \geq 0.35$, where $\frac{\mu_g}{\mu}$ is the gas to liquid viscosity ratio, V_g is the jet velocity and V_0 is the initial droplet impact velocity.

ACKNOWLEDGMENT

This work was supported by funding from the James R. Birle Endowment to the senior author Dr. Alfonso Ortega.

REFERENCES

[1] J. Kim, International Journal of Heat and Fluid Flow **28**, 753 (2007).

[2] L. C. Chow, M. S. Sehmbey, and M. R. Pais, Annual Review of Heat Transfer **8** (1997).

[3] M. Ebrahim and A. Ortega, Experimental Thermal and Fluid Science **80**, 168 (2017).

[4] A. J. Diaz and A. Ortega, Journal of Fluids Engineering **138**, 081104 (2016).

[5] C. Stow and M. Hadfield, Proceedings of the Royal Society of London. A. Mathematical and Physical Sciences **373**, 419 (1981).

[6] C. Mundo, M. Sommerfeld, and C. Tropea, International journal of multiphase flow **21**, 151 (1995).

[7] R. Rioboo, M. Marengo, and C. Tropea, Experiments in fluids **33**, 112 (2002).

[8] S. Sikalo, M. Marengo, C. Tropea, and E. Ganic, Experimental thermal and fluid science **25**, 503 (2002).

[9] S. Sikalo and E. Ganic, Experimental thermal and fluid science **31**, 97 (2006).

[10] L. Xu, W. W. Zhang, and S. R. Nagel, Physical review letters **94**, 184505 (2005).

[11] J. H. Moon, J. B. Lee, and S. H. Lee, Materials Transactions **54**, 260 (2013).

[12] R. Rioboo, C. Tropea, and M. Marengo, Atomization and Sprays **11** (2001).

[13] A. Yarin, Annu. Rev. Fluid Mech. **38**, 159 (2006).

[14] R.-H. Chen, L. C. Chow, and J. E. Navedo, International Journal of Heat and Mass Transfer **45**, 4033 (2002).

[15] W. Jia and H.-H. Qiu, Experimental Thermal and Fluid Science **27**, 829 (2003).

[16] Y. Son, C. Kim, D. H. Yang, and D. J. Ahn, Langmuir **24**, 2900 (2008).

[17] A. J. Diaz and A. Ortega, International journal of heat and mass transfer **67**, 1181 (2013).

[18] A. M. Briones, J. S. Ervin, S. A. Putnam, L. W. Byrd, and L. Gschwender, Langmuir **26**, 13272 (2010).

[19] X. He and L.-S. Luo, Physical Review E **56**, 6811 (1997).

[20] A. K. Gunstensen, D. H. Rothman, S. Zaleski, and G. Zanetti, Physical Review A **43**, 4320 (1991).

[21] M. R. Swift, W. Osborn, and J. Yeomans, Physical review letters **75**, 830 (1995).

[22] X. Shan and H. Chen, Physical Review E **47**, 1815 (1993).

[23] X. He, S. Chen, and R. Zhang, Journal of Computational Physics **152**, 642 (1999).

[24] L. Chen, Q. Kang, Y. Mu, Y.-L. He, and W.-Q. Tao, International journal of heat and mass transfer **76**, 210 (2014).

[25] X. He, X. Shan, and G. D. Doolen, Physical Review E **57**, R13 (1998).

[26] N. F. Carnahan and K. E. Starling, The Journal of Chemical Physics **51**, 635 (1969).

[27] A. R. Davies, J. L. Summers, and M. C. T. Wilson, International Journal of Computational Fluid Dynamics **20**, 415 (2006).

[28] D. Iwahara, H. Shinto, M. Miyahara, and K. Higashitani, Langmuir **19**, 9086 (2003).

[29] S. Chandra and C. Avedisian, Proceedings of the Royal Society of London. Series A: Mathematical and Physical Sciences **432**, 13 (1991).

[30] M. Pasandideh Fard, Y. Qiao, S. Chandra, and J. Mostaghimi, Physics of Fluids (1994-present) **8**, 650 (1996).

[31] W.-J. Yang, Tokyo, University, Institute of Space and Aeronautical Science, Report no. 535 **40**, 423 (1975).

[32] H. Jones, Journal of Physics D: Applied Physics **4**, 1657 (1971).

[33] J. Madejski, International journal of heat and mass transfer **19**, 1009 (1976).

[34] P. Attane, F. Girard, and V. Morin, Physics of Fluids **19**, 012101 (2007).

[35] S. Bechtel, D. Bogy, and F. Talke, IBM Journal of Research and Development **25**, 963 (1981).

[36] H.-Y. Kim and J.-H. Chun, Physics of Fluids (1994-present) **13**, 643 (2001).

[37] B. L. Scheller and D. W. Bousfield, AIChE Journal **41**, 1357 (1995).

[38] J. Drelich, E. Chibowski, D. D. Meng, and K. Terpilowski, Soft Matter **7**, 9804 (2011).

[39] J. Bico, U. Thiele, and D. Qur, Colloids and Surfaces A: Physicochemical and Engineering Aspects **206**, 41 (2002).

[40] D. Nuyttens, K. Baetens, M. De Schampheleire, and B. Sonck, Biosystems Engineering **97**, 333 (2007).

[41] J. Yang, L. Chow, and M. Pais, Journal of Heat Transfer **118**, 668 (1996).

[42] C. Chang, C.-H. Liu, and C.-A. Lin, Computers and Mathematics with Applications **58**, 940 (2009).

[43] C.-H. Liu, K.-H. Lin, H.-C. Mai, and C.-A. Lin, Computers and Mathematics with Applications **59**, 2178 (2010).

[44] A. Gupta, T. Damm, C. Cook, S. Charagundla, and C. Presser, in *35th Aerospace Science Meeting, Reno, NV*, pp. 97–0268.